
 Cite this: *Nanoscale*, 2021, **13**, 3817

Hydrogen-substituted graphdiyne/graphene as an sp/sp² hybridized carbon interlayer for lithium–sulfur batteries†

 Suzhen Kong,^a Dong Cai,^a Guifa Li,^b Xiangju Xu,^{*a} Suya Zhou,^a Xinwei Ding,^a Yongqin Zhang,^b Shuo Yang,^{a,c} Xuemei Zhou,^a Huagui Nie,^a Shaoming Huang,^{id d} Ping Peng^e and Zhi Yang^{id *a}

To overcome the shuttle effect in lithium–sulfur (Li–S) batteries, an sp/sp² hybridized all-carbon interlayer by coating graphene (Gra) and hydrogen-substituted graphdiyne (HsGDY) with a specific surface area as high as 2184 m² g⁻¹ on a cathode is designed and prepared. The two-dimensional network and rich pore structure of HsGDY can enable the fast physical adsorption of lithium polysulfides (LiPSs). *In situ* Raman spectroscopy and *ex situ* X-ray photoelectron spectroscopy (XPS) combined with density functional theory (DFT) computations confirm that the acetylenic bonds in HsGDY can trap the Li⁺ of LiPSs owing to the strong adsorption of Li⁺ by acetylenic active sites. The strong physical adsorption and chemical anchoring of LiPSs by the HsGDY materials promote the conversion reaction of LiPSs to further mitigate the shuttling problem. As a result, Li–S batteries integrated with the all-carbon interlayers exhibit excellent cycling stability during long-term cycling with an attenuation rate of 0.089% per cycle at 1 C over 500 cycles.

 Received 3rd November 2020,
 Accepted 28th December 2020

DOI: 10.1039/d0nr07878f

rsc.li/nanoscale

Introduction

Lithium–sulfur (Li–S) electrochemical systems are promising candidates for rechargeable batteries owing to their high energy density of 2600 W h kg⁻¹ and cost-effectiveness.^{1–3} Elemental sulfur has high natural abundance and low toxicity, and is of low cost, which contribute to the interest in developing Li–S battery technologies.^{4–6} However, sulfur cathodes operate by multi-electron transfer oxidation–reduction reactions, which produce soluble intermediate lithium polysulfides (LiPSs) that diffuse through the separator and directly react with the lithium anode.⁷ These effects cause irreversible loss of active materials, low coulombic efficiency, and poor cyclability.⁸ Moreover, the low electrical and ionic conductivities of

the sulfur species give rise to high overpotentials and low use of active materials.⁹ Therefore, trapping and reactivating LiPSs at the cathode side and promoting their conversion reactions are major challenges for Li–S batteries.^{10–12}

One strategy to address the issue of LiPS shuttling is to insert an interlayer between the cathode and separator.¹³ Manthiram *et al.* developed a microporous carbon interlayer to improve the cycling performance of Li–S batteries.¹⁴ Subsequently, carbon nanotubes (CNTs),¹⁵ carbon nanofibers,¹⁶ and graphene (Gra)¹⁷ have been used as interlayer materials. Carbon interlayers have a nonpolar surface, which means that they cannot trap soluble LiPSs by chemical adsorption.¹⁸ Hence, many researchers have attempted to increase the interaction energy with soluble LiPSs by introducing polar functional groups onto the surface of carbon interlayers.¹⁹ Inorganic materials including TiO₂,²⁰ MnO₂,²¹ V₂O₅,²² and MoS₂²³ are decorated over the carbon freestanding film to prevent polysulfide diffusion through strong chemisorption.²⁰ Even if LiPS shuttling is effectively inhibited, a dense functional layer covers the porous structure of the interlayer and impedes Li⁺ transfer.²⁴ Additionally, transition metal cations of inorganic materials dissolved in the liquid electrolyte, migrate to the anode, and deposit on their surface destroying the solid electrolyte interface membrane.¹⁹ These behaviors increase the resistance of the battery and degrade the battery cycle life. Thus, there is a need for a novel material to act as an all-carbon interlayer. Such an interlayer material should shield

^aKey Laboratory of Carbon Materials of Zhejiang Province, Wenzhou University, Wenzhou 325035, China. E-mail: xuxj@wzu.edu.cn, yang201079@126.com

^bSchool of Material Science and Engineering, Nanchang Hangkong University, Jiangxi, 330063, China

^cCollege of Electrical and Electronic Engineering, Wenzhou University, Wenzhou 325035, China

^dSchool of Materials and Energy, Guangdong University of Technology, Guangzhou 510006, China

^eSchool of Material Science and Engineering, Hunan University, Hunan, 410082, China

†Electronic supplementary information (ESI) available. See DOI: 10.1039/d0nr07878f

against physical and chemical adsorption to prevent LiPS shuttling.²⁵

Graphdiyne is a two-dimensional carbon allotrope formed by the combination of sp and sp² hybridized carbon atoms.²⁶ As a novel carbon-based nanomaterial with a planar network structure, graphdiyne has many unique properties and promising applications in energy-related fields.²⁷ Owing to the presence of sp hybridized carbon atoms, graphdiyne has a well-distributed pore structure and a large π -conjugated system.²⁸ The pore structure of graphdiyne materials can be precisely controlled to physically block the diffusion of LiPSs while enabling the diffusion of Li⁺.²⁹ There are many acetylenic units in graphdiyne materials and the lithiophilicity of acetylenic bonds is beneficial for trapping LiPSs by chemical adsorption.³⁰ Because of its unique structure, a graphdiyne interlayer might be expected to realize efficient immobilization and catalytic conversion of soluble LiPS intermediates. However, there have been few reports related to the use of graphdiyne interlayers in Li-S batteries.

In this work, we synthesized a hydrogen-substituted graphdiyne (HsGDY) material, which had a specific surface area as high as 2184 m² g⁻¹. We prepared functional Li-S batteries with a HsGDY/Gra interlayer to take advantage of synergetic effects between HsGDY and Gra. *In situ* Raman analysis and *ex situ* X-ray photoelectron spectroscopy (XPS) indicated that the strong adsorption ability of Li⁺ by acetylenic active sites contributed to the chemical anchoring of LiPSs. We further confirmed this mechanism through density functional theory (DFT) calculations. The strong physical adsorption and chemical anchoring of LiPSs by the HsGDY material promoted LiPSs conversion during the charge and discharge processes. Consequently, Li-S batteries with the HsGDY/Gra interlayer exhibited excellent cycling stability. After 500 cycles at a current density of 1 C, the attenuation rate was 0.089% per cycle. These results will guide the design of new high-performance interlayer materials for Li-S batteries.

Results and discussion

Synthesis and characterization of HsGDY

In this work, a porous, high specific surface area of HsGDY was obtained by a copper-catalyzed cross-coupling reaction, as shown schematically in Fig. 1a. HsGDY with sp-hybridized acetylenic bonds and sp²-hybridized benzene rings was demonstrated to be a semiconductor. Hence, Gra was selected to improve the conductivity of the system. To study its effects on the performance of Li-S batteries, HsGDY was physically mixed with Gra and used as an interlayer between the cathode and separator of the battery to form a CNTs-S@Gra-HsGDY configuration (Fig. 1b). It is noted that the Gra used here also plays a pivotal role in film-forming, and it makes the Gra-HsGDY interlayer membrane more compact and smooth, as shown in Fig. S1 (ESI[†]). It is beneficial to maintain the interlayer structure stability and make the dispersion of active sites

uniform. For comparison, Gra and HsGDY were also separately used as interlayers to form CNTs-S@Gra and CNTs-S@HsGDY, respectively.

Fig. 2a and b, together with Fig. S2 and S3 (ESI[†]), show the scanning electron microscopy (SEM) and transmission electron microscopy (TEM) images of HsGDY with a photograph of HsGDY in the inset of Fig. 2b. The photograph shows that the as-formed product was obtained as a brown powder rather than a film. The SEM and TEM images show that the samples had a continuous two-dimensional network and stacked structure with a large number of pores. The porous structure of the samples was further investigated by nitrogen adsorption-desorption measurements. From the insets in Fig. 2c, the main pore size distributions for HsGDY were located at 0.6 and 3 nm, corresponding to the micropores and mesopores, respectively. Considering the particle size of LiPSs, our micro/mesoporous HsGDY may efficiently restrain the shuttle of LiPSs by physical interactions.^{31,32} Furthermore, these pores contribute to form a large specific surface area. The Brunauer-Emmett-Teller (BET) surface area of the sample is 2184 m² g⁻¹. Such a specific surface area is impressively higher than almost all of the reported graphdiyne materials,³³⁻³⁶ showing great promise for applications. In a previous report,³⁷ copper acts as both a catalyst and substrate, and the film and nanosheets are formed by the layer-by-layer deposition of graphdiyne on the copper plate. Here, copper only serves as the catalyst source. In the reaction, in the presence of pyridine, a small amount of copper ions generated on the surface of copper foil and dissolved into the solution under stirring. The copper ions can form catalytically active sites, when the monomer is introduced by dripping. It reacted at these catalytically active sites, forming some HsGDY fragments. As the reaction progressed, more fragments are generated and assembled together, and the porous material is finally constructed in the solution. By controlling the experimental conditions, the aggregation structure of HsGDY can be well adjusted, which has a great influence on the specific surface area of the product.

The as-prepared samples were firstly characterized by XPS studies. The spectra confirmed the presence of C, O, and N elements in the samples (Fig. S4 in the ESI[†]). The C 1s peaks of HsGDY in Fig. 2d could be fitted into four subpeaks, corresponding to the sp² hybrid carbon (benzene rings) at 284.5 eV and the sp hybrid carbon (C≡C) at 285.2 eV.³⁵ These peaks had an area ratio close to 1 : 1, which is consistent with a previous report on HsGDY.³⁸ The peaks at 286.7 and 288.8 eV are assigned to C-O and C=O, respectively. The presence of the C-O and C=O bonds might be attributed to the chemical adsorption of oxygen on the surface of the sample, which was also observed in other carbon materials. The Raman spectrum in Fig. 2e features four distinct peaks. In addition to the G and D peaks, C≡C peaks were also observed at about 2046.8 and 2219.3 cm⁻¹.³⁹ The peak at 2207.8 cm⁻¹ of the Fourier-transform infrared (FT-IR) spectrum in Fig. 2f reconfirmed the existence of the C≡C bond. These aforementioned results strongly confirmed the successful synthesis of HsGDY with a specific

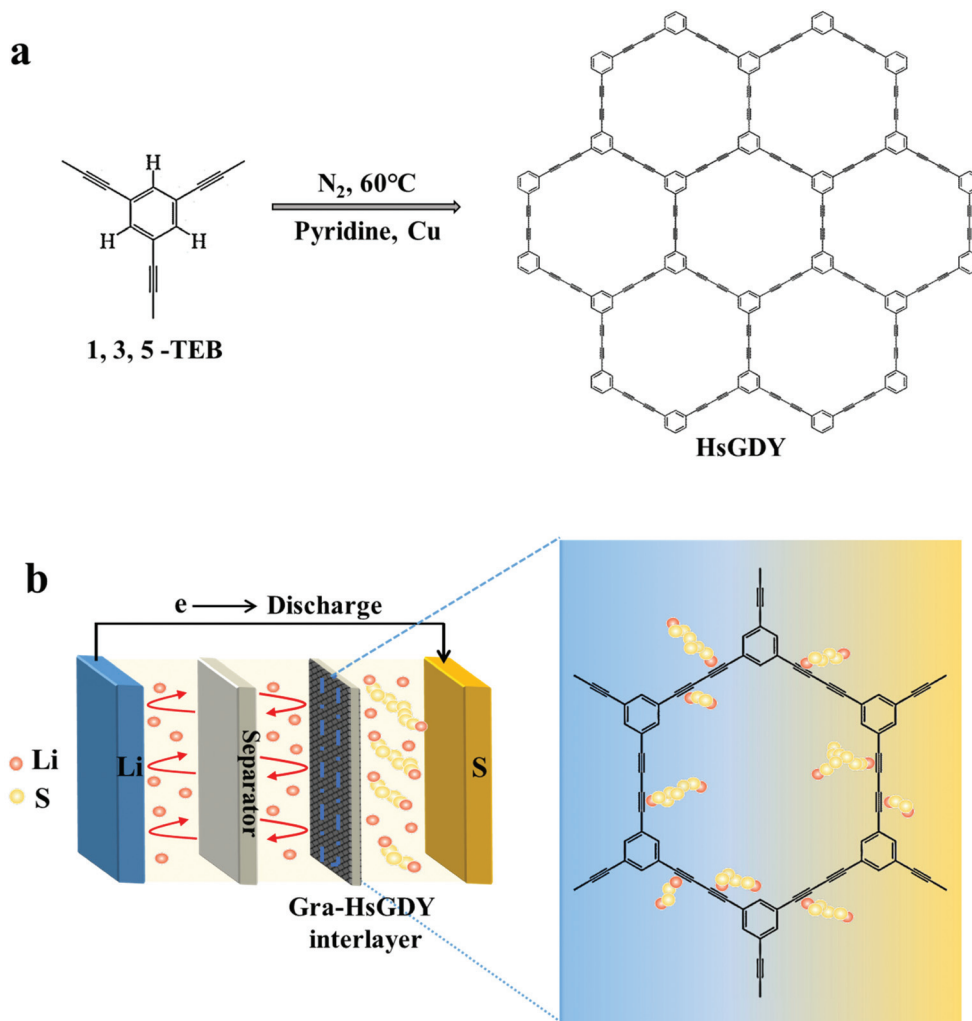


Fig. 1 (a) Synthesis scheme of HsGDY. (b) Schematic of a Li–S battery modified with a Gra–HsGDY interlayer.

surface area as high as $2184 \text{ m}^2 \text{ g}^{-1}$ through the copper ion-catalyzed coupling reaction.

Electrochemical performance

We examined the effects of introducing HsGDY into a battery interlayer on the performance of a CNTs–S cathode by comparing with the baseline of CNTs–S (Fig. S5 and S6 in the ESI†). Electrochemical studies suggested an optimal battery performance at a Gra to HsGDY mass ratio of 1 : 1. It is suggested that this CNTs@Gra–HsGDY carbon film provides almost no capacity contribution to CNTs–S@Gra–HsGDY (Fig. S7 in ESI†). Here, we denote the electrode with a Gra to HsGDY mass ratio of 1 : 1 as CNTs–S@Gra–HsGDY. The rate capacities of CNTs–S@Gra, CNTs–S@HsGDY, and CNTs–S@Gra–HsGDY at rates from 0.2 to 2 C ($1 \text{ C} = 1675 \text{ mA h g}^{-1}$) are shown in Fig. 3a. Compared with the other two samples, CNTs–S@Gra–HsGDY showed a higher discharge capacity of 1267, 963, 919, and 853 mA h g^{-1} at 0.2, 0.5, 1, and 2 C, respectively. Conversely, the initial capacity of CNTs–S@Gra and CNTs–S@HsGDY decreased to 1133 and 1039 mA h g^{-1} at 0.2 C, respectively.

When the current density was returned to 0.2 C, the capacity of CNTs–S@Gra–HsGDY recovered to 947 mA h g^{-1} (Fig. 3a). The excellent rate performance and good recovery of capacity suggested the high reversibility of CNTs–S@Gra–HsGDY. The galvanostatic charge–discharge profiles of the three samples at a current rate of 0.2 C are shown in Fig. 3b. These curves show that CNTs–S@Gra–HsGDY possesses a lower voltage hysteresis (ΔE) than the other two samples (Fig. 3b, Fig. S8 and S9 in the ESI†). The voltage hysteresis (ΔE) of CNTs–S@HsGDY was larger than that of CNTs–S@Gra, probably attributing to the lower conductivity of HsGDY than that of Gra.

To assess the electrochemical performance of these Li–S batteries, CNTs–S@Gra, CNTs–S@HsGDY, and CNTs–S@Gra–HsGDY were cycled in the potential range of 1.6–2.8 V at a scan rate of 0.1 mV s^{-1} , as shown in Fig. 3c and Fig. S10 (ESI†). During the cathodic scans, two characteristic reduction peaks were observed. The peaks at about 2.28 (P_1) and 2.01 V (P_2) can be attributed to the transformation of elemental sulfur (S_8) to long-chain LiPSs (Li_2S_n , $4 < n \leq 8$) and further to insoluble $\text{Li}_2\text{S}_2/\text{Li}_2\text{S}$, respectively.⁴⁰ In the subsequent anodic

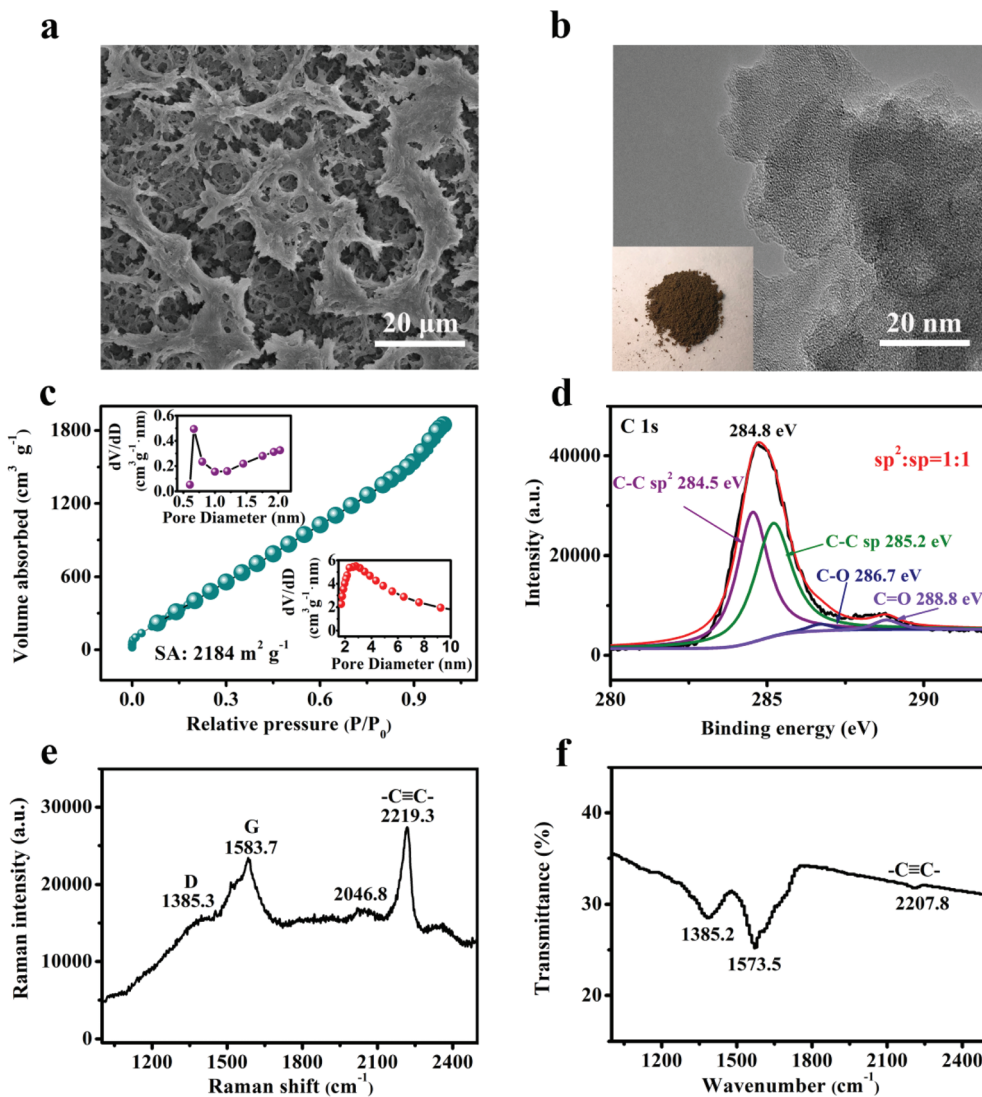


Fig. 2 The morphology and structure of HsGDY. (a) SEM image of HsGDY. (b) TEM image of HsGDY, the inset shows the photograph of the sample. (c) Nitrogen adsorption–desorption isotherm; pore size distributions are shown in the inset. (d) XPS spectrum of HsGDY. (e) Raman spectrum of HsGDY. (f) FT-IR spectrum of HsGDY.

scans, the peaks at about 2.26 (P_3) and 2.41 V (P_4) are assigned to the transformation from Li_2S to LiPSs and eventually to elemental sulfur.⁴¹ A slight variation in the reduction and oxidation peaks during the initial cycles may be attributed to the rearrangement of active sulfur from its original position to more energetically stable sites.⁴² After several cycles, the redox peaks of CNTs-S@Gra-HsGDY are well overlapped, which indicates its highly reversible electrochemical properties. The CV curves of CNTs-S@Gra , CNTs-S@HsGDY , and CNTs-S@Gra-HsGDY , in the fourth cycle, are chosen to emphasise the advantage of the Gra-HsGDY interlayer (Fig. 3d). The inset of Fig. 3d shows that CNTs-S@Gra-HsGDY has a more positive initial potential. The first reduction peak is attributed to the transition of S_8 to long-chain LiPSs , which suggests that sulfur species undergo fast redox reactions. Table S1 (ESI†) summarizes the polarized voltage (ΔV) and collects the coefficient

(I_L/I_H , I_L is the oxidative peak current and I_H is the reductive peak current) of the CNTs-S@Gra , CNTs-S@HsGDY , and CNTs-S@Gra-HsGDY samples. The results indicated the highest collection coefficient and the lowest polarized voltage of CNTs-S@Gra-HsGDY . These observations suggested that the introduction of HsGDY interlayers not only reduced the potential polarization of the battery system but also effectively promoted the conversion of sulfur to inhibit the shuttling effect and thus obtain a high reversible capacity.

One important factor for evaluating the performance of Li-S batteries is cycling stability. The long-term cycling profiles of CNTs-S@Gra , CNTs-S@HsGDY , and CNTs-S@Gra-HsGDY at 1 C are illustrated in Fig. 3e. The discharge capacity of CNTs-S@Gra-HsGDY was maintained at 554 mA h g^{-1} after 500 cycles with a negligible decay rate of 0.089% per cycle. This performance is comparable to that of other high-energy

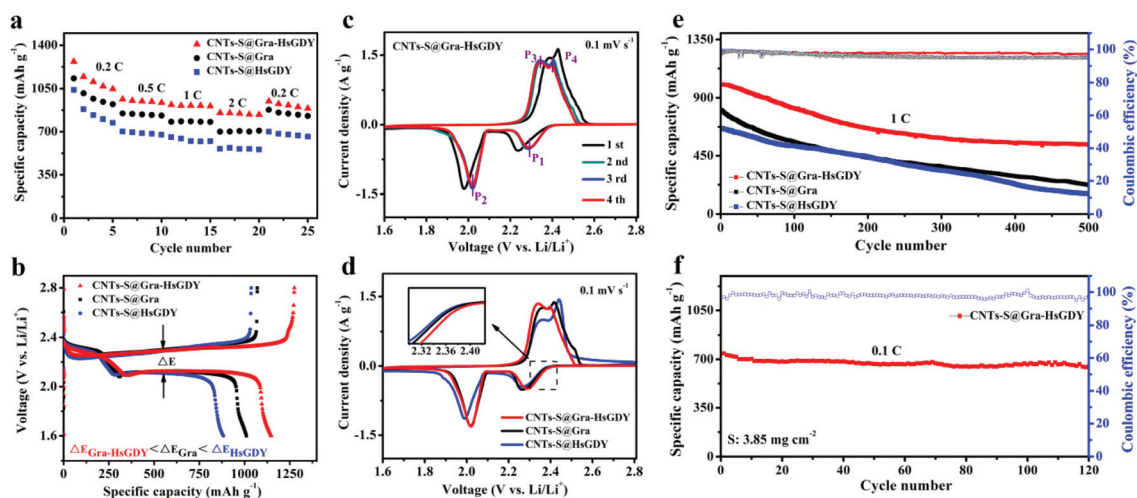


Fig. 3 Electrochemical performance of Li-S batteries. (a) The rate capabilities of CNTs-S@Gra-HsGDY, CNTs-S@Gra, and CNTs-S@HsGDY. (b) Galvanostatic charge–discharge profiles of the three cathodes at 0.2 C in the second cycle. (c) CV profiles of the CNTs-S@Gra-HsGDY-cathode between 1.6 and 2.8 V for the first four cycles, recorded at a scan rate of 0.1 mV s⁻¹. (d) The fourth cycle of CV profiles for CNTs-S@Gra-HsGDY, CNTs-S@Gra, and CNTs-S@HsGDY. The inset shows a higher magnification of the reduction current between 2.29 and 2.42 V. (e) Cycling performance of CNTs-S@Gra-HsGDY, CNTs-S@Gra, and CNTs-S@HsGDY over 500 cycles at 1 C. (f) Cycling stability of CNTs-S@Gra-HsGDY with a sulfur mass loading of 3.85 mg cm⁻² measured at a rate of 0.1 C for 120 cycles.

lithium batteries (Table S2 in the ESI[†]). For practical applications, CNTs-S@Gra-HsGDY with a higher sulfur loading of 3.85 mg cm⁻² was prepared. As shown in Fig. 3f, CNTs-S@Gra-HsGDY showed a high capacity retention rate of 87% at 0.1 C for over 120 cycles. Furthermore, the performance under lean electrolyte conditions (E/S ratio of 20, 15, and 10 mL g⁻¹) was also obtained (Fig. S11 in the ESI[†]) which showed only a slight decay. Increasing the sulfur loading to 5.2 mg cm⁻², CNTs-S@Gra-HsGDY still maintained superior performance (Fig. S12 in the ESI[†]). These results indicate that the use of HsGDY as an interlayer material of Li-S batteries improved the rate performance and cycling stability, thus showing good potential for practical applications.

Mechanism of HsGDY in Li-S batteries

XPS is a useful technique for studying the surface layer composition of interlayers under different discharge and charging conditions.⁴³ To explore the mechanism of performance enhancement in the battery after the introduction of HsGDY in CNTs-S@Gra-HsGDY, we performed *ex situ* XPS experiments for the CNTs-S@Gra-HsGDY and CNTs-S@Gra samples. Fig. 4a and b show the Li 1s XPS peaks of CNTs-S@Gra-HsGDY and CNTs-S@Gra from Li-S batteries discharged and charged to different states, (including the fully charged state at 2.4 V, half-discharged state at 2.1 V, fully discharged state at 1.6 V, half-charged state at 2.1 V, and fully charged state at 2.4 V) during the fifth cycle. The Li 1s spectra of CNTs-S@Gra-HsGDY (Fig. 4a) show that the Li 1s peak shifted from 55.8 to 56.0 eV during the discharge and shifted back again during charging. In a control experiment, *ex situ* XPS measurements show almost no shift of the Li 1s peak for CNTs-S@Gra during the discharge and charge processes. These findings suggest that

the introduction of HsGDY into CNTs-S@Gra-HsGDY affected the chemical state of Li⁺ in the battery. XPS survey spectra of CNTs-S@Gra-HsGDY after cycling are shown in Fig. S13. (ESI[†]). Specifically, Fig. 4c shows the high-resolution XPS spectra of the C 1s region fitted into five sub-peaks, corresponding to C–C (sp²), C–C (sp), C–S, C–O, and C=O. Notably, the area ratio of sp² to sp hybridized carbon (sp²:sp) gradually increased during the discharge process and decreased during the charging process. These results suggest an interaction and electron transfer between the acetylenic bonds and Li⁺ during the charge and discharge processes.

In situ Raman spectroscopy was used to examine the variation of acetylenic bonding and to better understand the interaction between Li⁺ and the acetylenic bond.⁴⁴ Fig. 5 shows the two sets of *in situ* Raman spectra recorded for the HsGDY electrode at various potentials during discharge and charge. As shown in Fig. 5a and b(i), the C≡C Raman peaks slightly shifted to higher wavenumbers during the cathodic scan and returned to lower wavenumbers during the anodic scan (Fig. 5c and d(i)). According to previous reports,^{45–48} HsGDY strongly binds with alkali metal ions and the shift of the Raman peak of C≡C is attributed to coupling with the electron donor. Thus, the observed shifts confirm the interactions between the acetylenic bonds and Li⁺, consistent with the XPS results. The intensity of the C≡C peak is plotted as a function of the battery potential in Fig. 5b(ii) and d(ii). The intensity of the peak was normalized by setting the integral area of C≡C at 2.8 V to 1. Fig. 5b(ii) shows that during the discharge process from 2.4 to 2.0 V, the peak intensity of the acetylenic bond sharply changed. This discharge range corresponds to the conversion of S₈ to LiPSs (Li₂S₈ → Li₂S₄ → Li₂S₂), which is the main region of Faraday current exchange based on the CV

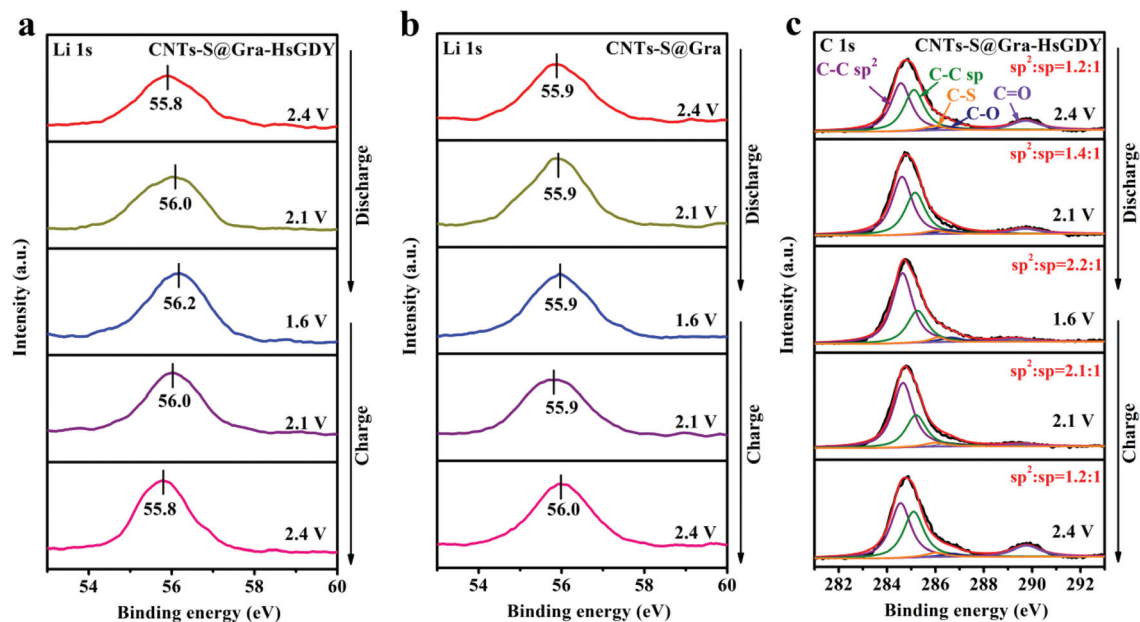


Fig. 4 Study of chemical interactions between HsGDY and Li^+ . *Ex situ* XPS spectra of the (a) Li 1s of CNTs-S@Gra-HsGDY and (b) Li 1s of CNTs-S@Gra. (c) XPS narrow scan for C 1s of CNTs-S@Gra-HsGDY at five different discharge/charge states: a fully charged state at 2.4 V, a half discharged state at 2.1 V, a fully discharged state at 1.6 V, a half charged state at 2.1 V, and a fully charged state at 2.4 V.

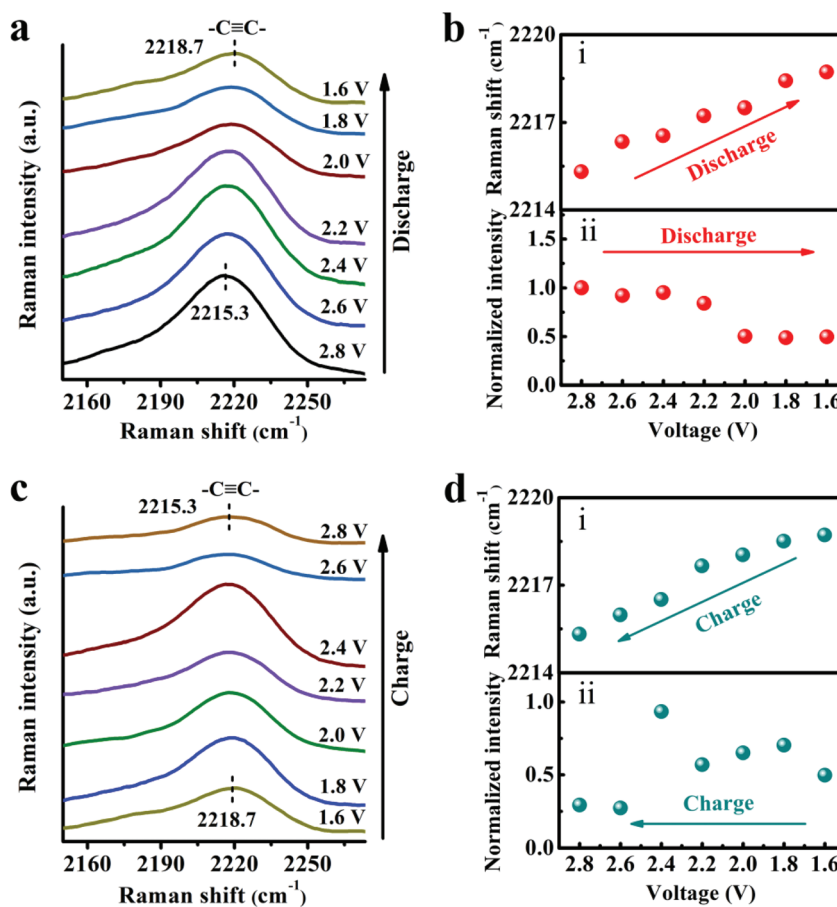


Fig. 5 Investigation of the interaction between HsGDY and Li^+ . *In situ* Raman spectra of the HsGDY electrode shown at respective potentials during (a) discharge from 2.8 V to 1.6 V and (c) after recharging to 2.8 V. Potential dependence of the (b(i) and d(i)) wavenumber and (b(ii) and d(ii)) normalized peak intensity corresponding to the C=C peak.

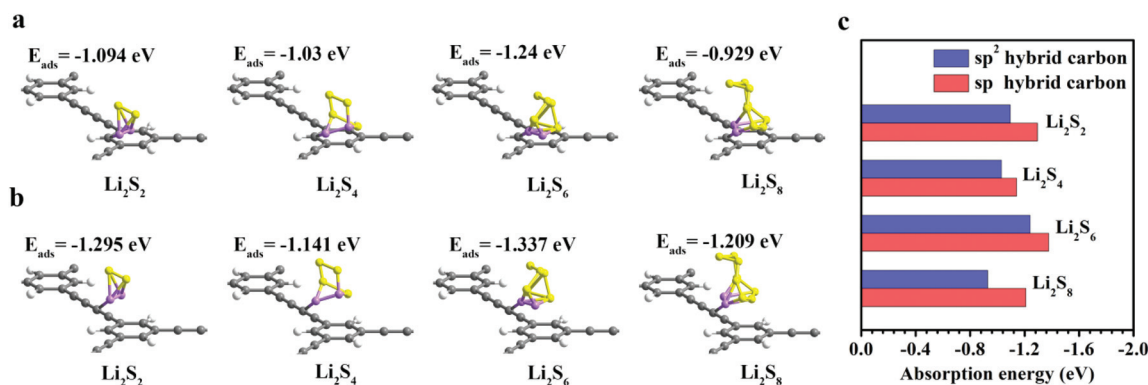


Fig. 6 Theoretical simulations the Li_2S_n ($n = 2, 4, 6, 8$) molecule adsorbed on HsGDY flakes. (a) The Li_2S_n molecule adsorbed on the sp^2 hybridized carbon of HsGDY. (b) The Li_2S_n molecule adsorbed on the sp hybridized carbon of HsGDY. (c) Calculated adsorption energies for Li_2S_n on the sp^2 hybridized carbon and sp hybridized carbon of HsGDY.

curve in Fig. 3c. As shown in Fig. 5d(ii), when the potential was scanned in a positive direction, the region where the intensity of the acetylenic bond peak changed most notably coincided with the position of S conversion. These results suggest that upon introduction of HsGDY into the Li-S battery system, HsGDY combined with the Li^+ of LiPSs and affected the conversion reaction of polysulfide ions.

To better understand the possible functionality of this HsGDY in Li-S batteries, especially the actual active sites for LiPSs, we conducted DFT simulations to explore the involved interactions. All calculations were performed with the plane-wave-based VASP code. The projector augmented wave (PAW) pseudopotentials were applied to describe electron-ion interactions. Moreover, the electronic exchange correlation effect was estimated using the local density approximation (LDA) functional. The Kohn-Sham one-electron valence states were expanded on the basis of plane waves with a cutoff energy of 400 eV. A mode containing 26 atoms (Fig. 6) was used to model its interactions with LiPSs. As shown in Fig. 6a and b, the sp and sp^2 hybridized carbon atoms of HsGDY could bind with various LiPSs through Li atoms. Specifically, the adsorption energies between sp^2/sp sites and Li_2S_2 , Li_2S_4 , Li_2S_6 , and Li_2S_8 are -1.094, -1.03, -1.24, and -0.929 eV and -1.295, -1.141, -1.337, and -1.209 eV, respectively, as shown in Fig. 6c and Table S3.† Notably, it is suggested that the sp^2 carbon atoms can also provide sites to trap LiPSs although the sp carbons are more efficiently due to the higher adsorption energy and the *ex/in situ* surveys. The static adsorption experiments in Fig. S14† show the synergistic effect. By combining with the abovementioned results, we speculate on the involved interaction mechanisms between HsGDY and LiPSs. The sp and sp^2 hybrid carbon atoms of HsGDY have the ability to effectively trap the Li atoms of LiPSs.⁴⁹ During the discharge process, Li atoms donated electrons to acetylenic bonds, resulting in the higher energy shifts of the Li 1s XPS spectra (Fig. 4a) and the $\text{C}\equiv\text{C}$ Raman peaks (Fig. 5a). Meanwhile, the π - π conjugation of the $\text{C}\equiv\text{C}$ bond is weakened (Fig. 4c).⁵⁰ Subsequently, the charging process exhibits a reverse trend,

giving a solid piece of evidence for the excellent reversibility of these active sites. Hence, the promotion of LiPSs adsorption and conversion by HsGDY could be expected.

Conclusions

In summary, we successfully designed and prepared an all-carbon interlayer for Li-S batteries by coating HsGDY and Gra on a cathode for the first time. The introduced film contained HsGDY with a specific surface area of up to $2184 \text{ m}^2 \text{ g}^{-1}$ and a rich pore structure enabled the fast physical adsorption of LiPSs at the interlayer surface. Our *ex situ* XPS, *in situ* Raman spectroscopy, and DFT computations confirmed that the acetylenic bonds in HsGDY trapped the Li^+ of LiPSs owing to their lithiophilicity. This behavior promoted the conversion reaction of the polysulfide ions to further mitigate the shuttling problem. Consequently, Li-S batteries with the all-carbon interlayer exhibited excellent cycling stability. After 500 cycles at a current density of 1 C, the attenuation rate was 0.089% per cycle. This novel all-carbon film with sp - sp^2 hybridization not only resolves some obstacles associated with Li-S batteries but also provides a new design strategy that may be applicable to other energy-storage systems such as lithium- O_2 batteries, electrocatalysis, and supercapacitors.

Experimental

Synthesis of hydrogen-substituted graphdiyne

1,3,5-Triethynylbenzene (98%), copper foil (99.8%, 0.025 mm thick), and pyridine (99.8%) were purchased from Sigma-Aldrich. All the chemical reagents were used without further purification. HsGDY was obtained following the synthesis route as shown in Fig. 1a. The copper foil (2 cm \times 2 cm) was cleaned ultrasonically in 1 M HCl, ethanol, and acetone successively for 10 minutes, and dried under a flow of nitrogen. The treated copper foil was immediately added to 50 mL of

pyridine in a flask. The mixture was stirred under a nitrogen atmosphere until the synthesis process is complete. In a typical synthesis, 12 mg of 1,3,5-triethynylbenzene was dissolved in 25 mL of pyridine and added slowly within 20 hours to the above solution. The synthesis was carried out under a nitrogen atmosphere at 60 °C for 2 days. After the reaction, the product was collected by vacuum filtration, and washed with heated acetone and *N,N*-dimethylformamide in turn to remove the unreacted monomer and oligomer and dried under nitrogen.

Synthesis of the CNTs-S cathode

The CNTs-S cathode was prepared by a conventional melting-diffusion treatment. In a typical procedure, commercial multi-walled CNTs (>95%, inside diameter: 3–5 nm, Aladdin) and sulfur powder (>99.99%, metal basis, Aladdin) were mixed in carbon disulfide (CS₂, >99.9%, Aladdin) solution at a mass ratio of 1 : 4, followed by heating at 155 °C for 12 hours. The CNTs-S cathode was prepared by blending 5 wt% PVDF, 10 wt% conductive materials, and 85 wt% CNT-S composite materials in *N*-methyl pyrrolidone (NMP) to form a slurry. After stirring for 2 hours, the slurry was cast on aluminum foil and dried at 55 °C overnight. The sulfur contents of CNT-S composites in this work were usually controlled between 75 and 80 wt%.

Synthesis of CNTs-S@Gra and CNTs-S@HsGDY

The Gra interlayer slurry was prepared by mixing Gra (>99%, diameter, 0.5–5 μm; thickness, ~0.8 nm; XFNANO) with *N,N*-dimethylformamide (Aladdin) solution and then the mixture was treated with ultrasonication. Subsequently, the Gra interlayer slurry was then pasted onto the CNT-S cathode and dried at 55 °C overnight to produce CNTs-S@Gra. The sulfur mass loading in the cathodes is about 1.2 mg cm⁻². The dried cathode was punched into a disk of 14 mm in diameter for assembling cells. CNTs-S@HsGDY was prepared by a similar operation, only replacing Gra by HsGDY.

Synthesis of CNTs-S@Gra-HsGDY

The Gra-HsGDY interlayer slurry was prepared by dispersing Gra and HsGDY into *N,N*-dimethylformamide solution at a mass ratio of 1 : 1 and then the mixture was subjected to ultrasonication. Subsequently, the Gra-HsGDY interlayer slurry was then pasted onto the CNT-S cathode and dried at 55 °C overnight to produce CNTs-S@Gra-HsGDY. The sulfur mass loading in the cathode is about 1.2 mg cm⁻², unless otherwise noted. The dried interlayer-on-cathode was punched into a disk of 14 mm diameter for assembling cells.

Electrochemical characterization

Electrochemical experiments were performed using CR2025 coin cells assembled in an argon-filled glove box with water and oxygen below 0.1 ppm. Lithium metal was used as the anode. A Celgard 2400 membrane was used as the separator to isolate electrons. The electrolyte was 1 M bis(trifluoromethane) sulfonimide lithium salt (LiTFSI) with 1 wt% LiNO₃ in 1,3-dioxolane (DOL)/1,2-dimethoxyethane (DME) (DOL/DME, 1 : 1

in volume, Suzhou DodoChem Ltd, China). The ratio of electrolyte/sulfur for the coin cell was about 25 : 1 (μL mg⁻¹). The areas of the anode and cathode are about 1.53 cm⁻². Discharge/charge measurement were performed in the potential range of 1.6–2.8 V (vs. Li/Li⁺) using a Neware battery test system (Shen Zhen Neware Technology Co. Ltd, China). Cyclic voltammetry was performed using a CHI760E electrochemical workstation (Shanghai Chenhua Instrument Co. Ltd, China). The CV was recorded at a scanning speed of 0.1 mV s⁻¹ between 1.6 and 2.8 V (vs. Li/Li⁺).

Structural characterization

A JSM-6700F field emission scanning electron microscope was used to obtain scanning electron microscopy (SEM) images. Transmission electron microscopy (TEM) images were obtained on a TECNAI G2F20 microscope. A micromeritics ASAP 2020 M device was used to record nitrogen adsorption/desorption isotherms at liquid nitrogen temperatures (77 K). Prior to the measurement, the sample was degassed at 200 °C under vacuum for 3 hours. The Barrett-Joyner-Halenda (BJH) model was used to derive the pore size distribution (PSD) from the adsorption branch of the isotherms. Total pore volumes were calculated from the amount adsorbed when the relative pressure (P/P_0) was 0.99. The Brunauer-Emmett-Teller (BET) equation was used to calculate the specific surface area. X-ray diffraction patterns (XRD) were recorded using a D/MAX-2400 diffractometer with Cu K α radiation (40 kV, 100 mA, $\lambda = 1.54056$ Å). X-ray photoelectron spectroscopy (XPS) measurements were obtained using an ultrahigh vacuum setup equipped with a monochromatic Al-K X-ray source and a high resolution Gammadata-Scienta SES 2002 analyzer. Thermogravimetric analysis (TGA) was performed using a STA449 F3 Jupiter gravimetric analyzer (NETZSCH) under a nitrogen atmosphere at a rate of temperature increase of 10 °C min⁻¹. Raman spectra were recorded with a Renishaw inVia Raman microscope using a 532 nm line of an Ar-ion laser. Fourier transform infrared (FT-IR) spectra were recorded using a Fourier-transform infrared spectrometer (iS50, Thermo Fisher).

X-ray photoelectron spectroscopy measurements

XPS experiments were performed using a Thermo Fisher Scientific K-Alpha spectrometer using monochromatic Al-K α X-rays as the excitation source (10 mA, 15 kV). The binding energy scale was calibrated to the C 1s peak near 284.8 eV. The diameter of the analysis area is about 500 μm, and the basic pressure of the instrument is 2×10^{-9} mbar. In order to determine the surface chemical state of the cathode produced under the Li-S battery cycle, the samples used for the *ex situ* XPS measurement were prepared by discharging (or recharging) the cathode in a certain state of discharge (or of charge), and then the glove box filled with argon was decomposed and sealed in a bottle, and then quickly transferred to the XPS chamber.

In situ Raman spectroscopy measurements

Raman spectra were recorded with a Renishaw inVia Raman microscope using a 532 nm laser under ambient conditions in

an airtight cell. An *in situ* electrochemical Raman cell was used in this study as reported previously.⁴² In short, the airtight cell consists of a polyethylene body and a glass carbon (GC) modified with GDY cathode materials as the working electrode, a Pt wire counter electrode, a Li₂S₈ electrolyte and a flat Pyrex glass window. The Li₂S₈ electrolyte was prepared by adding Li₂S and S at a molar ratio of 1:7 into dimethyl sulfoxide (DMSO, 99.9%, Aladdin) and stirring at 25 °C for 24 h in an argon atmosphere. The surface of the working electrode was positioned ~1 mm from the glass window. The cell was assembled in an argon-filled glovebox, and then fixed on a sample holder of the Raman microscope. It is pointed out that the cell assembly is not optimized for electrochemical performance as in the coin cell but rather to enable optical spectroscopy on the cathode while transporting lithium across the electrodes. *In situ* Raman measurements were carried out on a Renishaw inVia Raman spectrometer controlled using the WiRE 4.0 software. A laser of 532 nm and 50 mW vertically crosses the glass and was focused on the cathode surface with a 50× objective. The average acquisition time for each spectrum was 10 s. Electrochemical cycling was carried out using a CHI760E electrochemical workstation (Shanghai Chenhua Instrument Co. Ltd, China).

Computational details

Suggested by Kim *et al.*⁵¹ and Wang *et al.*,⁵² the adsorption ability of Li₂S_n ($n = 2, 4, 6, 8$) on HsGDY flakes is simulated by a first-principles pseudopotential planewave method implemented in the Cambridge Sequential Total Energy Package (CASTEP) software as shown in Fig. 6.⁵³ During optimization and total energy calculations, the electronic exchange–correlation energy functions were represented in reciprocal space with Perdew–Burke–Ernzerhof (PBE) functions, which were based on the generalized gradient approximation (GGA). The bulk geometries of HsGDY with and without the Li–S molecule were obtained from periodic calculations with PBE augmented by the D3 dispersion correction.^{54,55} All of the bulk surface models were built with a vacuum thickness greater than 15 Å to eliminate the interaction of two Li₂S_n ($n = 2, 4, 6, 8$) molecules. In this calculation, the cut-off energy of atomic wave functions, E_{cut} , was set at 400 eV. The special K-point in the Monkhorst–Pack scheme chosen as $1 \times 1 \times 2$ was used during the course of Brillouin zone integration. All atomic positions in these primitive cells were relaxed according to the total energy and force using the geometry optimization scheme improved by Broyden, Fletcher, Goldfarb, and Shanno *et al.* (BFGS),^{56–59} based on the cell optimization criteria (a root mean square (RMS) force of $0.1 \text{ eV } \text{Å}^{-1}$, a stress of 0.2 GPa, and a displacement of 0.005 Å). The convergence criteria of the self-consistent field and energy tolerances were set at 1.0×10^{-5} and 5.0×10^{-5} eV per atom, respectively.

The adsorption energy (E_{ads}) of Li₂S_n ($n = 2, 4, 6, 8$) molecules on HsGDY flakes was calculated as follows:

$$E_{\text{ads}} = -(E_{\text{total}} - E_{\text{HsGDY}} - E_{\text{Li-s}}).$$

Author contributions

Zhi Yang and Xiangju Xu conceived the idea and designed the experiments. Suzhen Kong performed the experiments and data processing and prepared the figures. Dong Cai, Suya Zhou, Xinwei Ding, Shuo Yang, Xuemei Zhou, Huagui Nie, and Shaoming Huang helped to analyze the data. Guifa Li, Yongqin Zhang and Ping Peng were responsible for density functional theory computations. Suzhen Kong, Xiangju Xu, and Zhi Yang co-wrote the paper. Xiangju Xu, Dong Cai and Zhi Yang were responsible for planning and supervising the project. All authors discussed the results and commented on the manuscript.

Conflicts of interest

There are no conflicts of interest to declare.

Acknowledgements

The work was supported in part by grants from the Natural Science Foundation of Zhejiang Province (LR18E020001 and LQ19B30006), the National Natural Science Foundation of China (51972238, 21875166, and 51920105004), the Major Research Plan of Wenzhou City (ZG2017027), and the Science and Technology Project of Zhejiang Province (LGF18B050005).

References

- 1 T. Hou, W. Xu, X. Chen, H. Peng, J. Huang and Q. Zhang, *Angew. Chem., Int. Ed.*, 2017, **56**, 8178–8182.
- 2 S. Shen, S. Zhang, S. Deng, G. Pan, Y. Wang, Q. Liu, X. Wang, X. Xia and J. Tu, *J. Mater. Chem. A*, 2019, **7**, 22958–22966.
- 3 X. Tao, J. Wang, C. Liu, H. Wang, H. Yao, G. Zheng, Z. W. Seh, Q. Cai, W. Li, G. Zhou, C. Zu and Y. Cui, *Nat. Commun.*, 2016, **7**, 11203.
- 4 J. Wu, X. Li, Z. Rao, X. Xu, Z. Cheng, Y. Liao, L. Yuan, X. Xie, Z. Li and Y. Huang, *Nano Energy*, 2020, **72**, 104725.
- 5 M. Zhao, H. Peng, Z. Zhang, B. Li, X. Chen, J. Xie, X. Chen, J. Wei, Q. Zhang and J. Huang, *Angew. Chem.*, 2019, **58**, 3779–3783.
- 6 H. Liu, S. Zhang, Q. Zhu, B. Cao, P. Zhang, N. Sun, B. Xu, F. Wu and R. Chen, *J. Mater. Chem. A*, 2019, **7**, 11205–11213.
- 7 G. Zhou, D. Wang, L. Li, N. Li, F. Li and H. Cheng, *Nanoscale*, 2013, **5**, 1576–1582.
- 8 X. Liang, Q. Pang, I. R. Kochetkov, M. S. Sempere, H. Huang, X. Sun and L. F. Nazar, *Nat. Energy*, 2017, **2**, 17119.
- 9 L. Zhou, M. K. Tufail, L. Yang, N. Ahmad, R. Chen and W. Yang, *Chem. Eng. J.*, 2020, **391**, 123529.
- 10 T. Chen, W. Kong, P. Zhao, H. Lin, Y. Hu, R. Chen, W. Yan and Z. Jin, *Chem. Mater.*, 2019, **31**, 7565–7573.
- 11 W. Shin, J. Lu and X. Ji, *Carbon Energy*, 2019, **1**, 165–172.

- 12 F. Liu, C. Wang, X. Sui, M. A. Riaz, M. Xu, L. Wei and Y. Chen, *Carbon Energy*, 2019, **1**, 173–199.
- 13 L. Jiao, S. Wu, Y. Tao, W. Lv, C. Zhang, G. Ling and Q. Yang, *Energy Storage Materials*, 2019, **23**, 112–136.
- 14 Y. S. Su and A. Manthiram, *Nat. Commun.*, 2012, **3**, 1166.
- 15 L. Sun, W. Kong, M. Li, H. Wu, K. Jiang, Q. Li, Y. Zhang, J. Wang and S. Fan, *Nanotechnology*, 2016, **27**, 075401.
- 16 S. Chung, P. Han, R. Singhal, V. Kalra and A. Manthiram, *Adv. Energy Mater.*, 2015, **5**, 1500738.
- 17 L. Wang, Z. Yang, H. Nie, C. Gu, W. Hua, X. Xu, X. Chen, Y. Chen and S. Huang, *J. Mater. Chem. A*, 2016, **4**, 15343–15352.
- 18 Z. Xiao, Z. Yang, H. Nie, Y. Lu, K. Yang and S. Huang, *J. Mater. Chem. A*, 2014, **2**, 8683–8689.
- 19 D. He, J. Meng, X. Chen, Y. Liao, Z. Cheng, L. Yuan, Z. Li and Y. Huang, *Adv. Funct. Mater.*, 2020, **30**, 2001201.
- 20 T. Zhou, W. Lv, J. Li, G. Zhou, Y. Zhao, S. Fan, B. Liu, B. Li, F. Kang and Q. Yang, *Energy Environ. Sci.*, 2017, **10**, 1694–1703.
- 21 W. Kong, L. Yan, Y. Luo, D. Wang, K. Jiang, Q. Li, S. Fan and J. Wang, *Adv. Funct. Mater.*, 2017, **27**, 1606663.
- 22 Z. A. Ghazi, X. He, A. M. Khattak, N. A. Khan, B. Liang, A. Iqbal, J. Wang, H. Sin, L. Li and Z. Tang, *Adv. Mater.*, 2017, **29**, 1606817.
- 23 Z. Zhang, G. Wu, H. Ji, D. Chen, D. Xia, K. Gao, J. Xu, B. Mao, S. Yi, L. Zhang, Y. Wang, Y. Zhou, L. Kang and Y. Gao, *Nanomaterials*, 2020, **10**, 705.
- 24 W. Chen, T. Lei, W. Lv, Y. Hu, Y. Yan, Y. Jiao, W. He, Z. Li, C. Yan and J. Xiong, *Adv. Mater.*, 2018, **30**, 1804084.
- 25 Z. Xiao, Z. Yang, L. Zhou, L. Zhang and R. Wang, *ACS Appl. Mater. Interfaces*, 2017, **9**, 18845–18855.
- 26 J. He, N. Wang, Z. Yang, X. Shen, K. Wang, C. Huang, Y. Yi, Z. Tu and Y. Li, *Energy Environ. Sci.*, 2018, **11**, 2893–2903.
- 27 N. Wang, J. He, Z. Tu, Z. Yang, F. Zhao, X. Li, C. Huang, K. Wang, T. Jiu, Y. Yi and Y. Li, *Angew. Chem., Int. Ed.*, 2017, **56**, 10740–10745.
- 28 J. Li, S. Li, Q. Liu, C. Yin, L. Tong, C. Chen and J. Zhang, *Small*, 2019, **15**, 1805344.
- 29 Y. Wang, J. He, Z. Zhang, Z. Liu, C. Huang and Y. Jin, *ACS Appl. Mater. Interfaces*, 2019, **11**, 35738–35745.
- 30 K. Wang, X. Li, N. Wang, Z. Yang, J. Gao, J. He, Y. Zhang and C. Huang, *ACS Appl. Energy Mater.*, 2020, **3**, 2623–2633.
- 31 X. Ji, K. T. Lee and L. F. Nazar, *Nat. Mater.*, 2009, **8**, 500–506.
- 32 M. Mazloumi, S. Shadmehr, Y. Rangom, L. F. Nazar and X. Tang, *ACS Nano*, 2013, **7**, 4281–4288.
- 33 T. Chen, W. Q. Li, X. J. Chen, Y. Z. Guo, W. B. Hu, W. J. Hu, Y. A. Liu, H. Yang and K. Wen, *Chem. – Eur. J.*, 2020, **26**, 2269–2275.
- 34 R. Sakamoto, R. Shiotsuki, K. Wada, N. Fukui, H. Maeda, J. Komeda, R. Sekine, K. Harano and H. Nishihara, *J. Mater. Chem. A*, 2018, **6**, 22189–22194.
- 35 C. Yang, Y. Li, Y. Chen, Q. Li, L. Wu and X. Cui, *Small*, 2019, **15**, 1804710.
- 36 X. Shen, X. Li, F. Zhao, N. Wang, C. Xie, J. He, W. Si, Y. Yi, Z. Yang, X. Li, F. Lu and C. Huang, *2D Mater.*, 2019, **6**, 035020.
- 37 G. Li, Y. Li, H. Liu, Y. Guo, Y. Li and D. Zhu, *Chem. Commun.*, 2010, **46**, 3256–3258.
- 38 J. He, N. Wang, Z. Cui, H. Du, L. Fu, C. Huang, Z. Yang, X. Shen, Y. Yi, Z. Tu and Y. Li, *Nat. Commun.*, 2017, **8**, 1172–1172.
- 39 J. Li, J. Xu, Z. Xie, X. Gao, J. Zhou, Y. Xiong, C. Chen, J. Zhang and Z. Liu, *Adv. Mater.*, 2018, **30**, 1800548.
- 40 W. Hua, Z. Yang, H. Nie, Z. Li, J. Yang, Z. Guo, C. Ruan, X. Chen and S. Huang, *ACS Nano*, 2017, **11**, 2209–2218.
- 41 Y. Lai, H. Nie, X. Xu, G. Fang, X. Ding, D. Chan, S. Zhou, Y. Zhang, X. Chen and Z. Yang, *ACS Appl. Mater. Interfaces*, 2019, **11**, 29978–29984.
- 42 D. Chan, Z. Xiao, Z. Guo, Y. Lai, Y. Zhang, S. Zhou, X. Ding, H. Nie and Z. Yang, *Nanoscale*, 2019, **11**, 16968–16977.
- 43 S. Zhou, S. Yang, X. Ding, Y. Lai, H. Nie, Y. Zhang, D. Chan, H. Duan, S. Huang and Z. Yang, *ACS Nano*, 2020, **14**, 7538–7551.
- 44 X. Ding, S. Yang, S. Zhou, Y. Zhan, Y. Lai, X. Zhou, X. Xu, H. Nie, S. Huang and Z. Yang, *Adv. Funct. Mater.*, 2020, **30**, 2003354.
- 45 J. Li, X. Gao, B. Liu, Q. Feng, X. Li, M. Huang, Z. Liu, J. Zhang, C. Tung and L. Wu, *J. Am. Chem. Soc.*, 2016, **138**, 3954–3957.
- 46 J. Wang, K. Wang, Z. Yang, X. Li, J. Gao, J. He, N. Wang, H. Wang, Y. Zhang and C. Huang, *ACS Sustainable Chem. Eng.*, 2019, **8**, 1741–1750.
- 47 J. Xiao, J. Shi, H. Liu, Y. Xu, S. Lv, Y. Luo, D. Li, Q. Meng and Y. Li, *Adv. Energy Mater.*, 2015, **5**, 1401943.
- 48 K. Wang, N. Wang, J. He, Z. Yang, X. Shen and C. Huang, *Electrochim. Acta*, 2017, **253**, 506–516.
- 49 Y. Zhao, L. Zhang, J. Qi, Q. Jin, K. Lin and D. Wang, *Acta Phys.-Chim. Sin.*, 2018, **34**, 1048–1060.
- 50 Y. Guo, J. Liu, Q. Yang, L. Ma, Y. Zhao, Z. Huang, X. Li, B. Dong, X. Z. Fu and C. Zhi, *Small*, 2020, **16**, 1907341.
- 51 J. Kim, S. Kang, J. Lim and W. Y. Kim, *ACS Appl. Mater. Interfaces*, 2019, **11**, 2677–2683.
- 52 F. Wang, Z. Zuo, L. Li, F. He and Y. Li, *Nano Energy*, 2020, **68**, 104307.
- 53 M. D. Segall, P. J. D. Lindan, M. J. Probert, C. J. Pickard, P. J. Hasnip, S. J. Clark and M. C. Payne, *J. Phys.: Condens. Matter*, 2002, **14**, 2717–2744.
- 54 S. Grimme, J. Antony, S. Ehrlich and H. Krieg, *J. Chem. Phys.*, 2010, **132**, 154104.
- 55 J. P. Perdew, K. Burke and M. Ernzerhof, *Phys. Rev. Lett.*, 1996, **77**, 3865–3868.
- 56 C. G. Broyden, *Mathematics of Computation*, 1965, **19**, 577–593.
- 57 R. Fletcher, *The Computer Journal*, 1970, **13**, 317–322.
- 58 D. Goldfarb, *Mathematics of Computation*, 1976, **30**, 796–811.
- 59 D. F. Shanno, *Mathematics of Computation*, 1970, **24**, 647–656.